Applied Catalysis B: Environmental 170-171 (2015) 293–300

Contents lists available at ScienceDirect

Applied Catalysis B: Environmental

journal homepage: www.elsevier.com/locate/apcatb

# Plasma-catalytic removal of formaldehyde over Cu–Ce catalysts in a dielectric barrier discharge reactor

Xinbo Zhu[a,b], Xiang Gao[a,**], Rui Qin[a], Yuxuan Zeng[b], Ruiyang Qu[a], Chenghang Zheng[a], Xin Tu[b,*]

[a] State Key Laboratory of Clean Energy Utilization, Zhejiang University, Hangzhou 310027, PR China
[b] Department of Electrical Engineering and Electronics, University of Liverpool, Liverpool L69 3GJ, UK

ARTICLE INFO

*Article history:*
Received 30 October 2014
Received in revised form 21 January 2015
Accepted 23 January 2015
Available online 24 January 2015

*Keywords:*
Plasma-catalysis
Dielectric barrier discharge (DBD)
Formaldehyde
Cu–Ce catalysts

ABSTRACT

In this study, a coaxial dielectric barrier discharge (DBD) reactor has been used for plasma-catalytic removal of low concentration formaldehyde over a series of Cu–Ce oxide catalysts prepared by the citric acid sol–gel method. The effect of the Cu/Ce molar ratio on the removal of formaldehyde and $CO_2$ selectivity has been investigated as a function of specific energy density (SED). In comparison to the plasma-only process, the combination of plasma with the Cu–Ce binary oxide catalysts significantly enhances the reaction performance, while the presence of CuO or $CeO_2$ in the DBD reactor has a negative effect on the removal of HCHO. This suggests that the interactions between Cu and Ce species change the properties of the catalysts and consequently affect the performance of the plasma-catalytic process. The highest removal efficiency of 94.7% and $CO_2$ selectivity of 97.3% were achieved when the Cu1Ce1 catalyst (Cu/Ce = 1:1) was placed in the DBD reactor at the SED of 486 J $L^{-1}$. The interaction between Cu and Ce species results in a larger specific surface area and pore volume, along with a greater formation of surface adsorbed oxygen ($O_{ads}$), which favors the oxidation of formaldehyde in the plasma process. In addition, the redox cycles between Cu and Ce species facilitate the formation of additional active oxygen atoms and contribute to the plasma-catalytic oxidation reactions. Plausible reaction mechanisms involved in the plasma-catalytic oxidation of HCHO have been proposed.



## 1. Introduction

Formaldehyde (HCHO) is a hazardous air pollutant that is mainly emitted from industrial processes such as the manufacturing of wood products and building materials, and combustion processes. As one of the toxic volatile organic compounds (VOCs), the emission of formaldehyde has become a great concern in our society due to its harmful effects on our health and environment, especially as a suspected carcinogen. Significant efforts have been devoted to the development and investigation of various pollution remediation technologies including adsorption, membrane separation, biological process, thermal combustion and catalytic oxidation for the removal of formaldehyde. However, conventional technologies are not cost-effective for the removal of low concentration VOCs (e.g., formaldehyde) in high volume waste gas streams. For example, thermal processes require large amounts of energy for heating the high volume gas flow to clean only a low concentration of environmental pollutants.

Non-thermal plasma (NTP) has been regarded as a promising method for the removal of a wide range of low concentration volatile organic compounds (VOCs) due to its non-equilibrium character, fast reaction, low energy cost and unique ability to initiate both physical and chemical reactions at low temperatures [1]. Energetic electrons generated in non-thermal plasma can collide with carrier gases, forming highly reactive species such as free radicals and excited atoms, molecules and ions. These species are capable of breaking most chemical bonds or initiating chemical reactions, leading to the removal of various VOC pollutants [2–5]. However, the selectivity toward the desired final products (e.g., $CO_2$ and $H_2O$) through deep oxidation is typically low when using plasma discharge alone, whilst the formation of unwanted by-products is inevitable [3,5]. Recently, a hybrid plasma-catalysis technology has been developed to combine the advantages of high selectivity from catalysis with the low temperature, fast reaction provided by non-thermal plasma [6–8]. The integration of plasma

* Corresponding author at: Department of Electrical Engineering and Electronics, University of Liverpool, Liverpool L69 3GJ, UK. Tel.: +44 1517944513.
** Corresponding author at: State Key Laboratory of Clean Energy Utilization, Zhejiang University, Hangzhou 310027, PR China.
*E-mail addresses:* xgao1@zju.edu.cn (X. Gao), xin.tu@liv.ac.uk (X. Tu).

http://dx.doi.org/10.1016/j.apcatb.2015.01.032
0926-3373/

and catalysis has great potential to reduce the operating temperature of catalyst activation, enhance the removal efficiency of the gas pollutant and increase the selectivity of the desired final products to minimise the formation of unwanted by-products (such as $NO_x$); all of which contribute to enhancing the energy efficiency of the process [8–10].

Catalysts are regarded as one of the most important factors to determine the reaction performance of a plasma-catalysis system. Different catalysts including $\gamma$-$Al_2O_3$, $TiO_2$, zeolite 13X and $NaNO_2$ coated raschig rings, have been shown to enhance the process performance for the plasma-catalytic oxidation of formaldehyde [11,12]. Ding et al. found that the presence of $Ag/CeO_2$ catalysts in a dielectric barrier discharge (DBD) significantly improved the removal efficiency of formaldehyde and $CO_2$ selectivity, which can be attributed to the formation of plasma-enhanced catalytic redox cycles between Ag and Ce species [13]. Zhao et al. also reported a similar interaction effect from Ag and Cu in the AgCu/HZSM-5 for formaldehyde removal in a cycled storage-discharge (CSD) system [14]. However, high costs of noble metals could limit the use of these catalysts for industrial applications. Up until now, the knowledge of supported metal oxide catalysts, especially the binary oxide catalysts, for the plasma-catalytic oxidation of formaldehyde is rather limited [15,16].

Cu-based catalysts have been widely used in the oxidation of VOCs due to their sufficient catalytic activity and relatively low cost [17]. Cerium oxide ($CeO_2$) has been regarded as an effective promoter in thermal catalytic reactions due to its high oxygen storage capacities and redox properties between $Ce^{4+}$ and $Ce^{3+}$. $CeO_2$ can also act as a local source/sink of oxygen species due to its high bulk oxygen mobility and oxygen vacancies [18]. Cu–Ce mixed oxides have been regarded as promising catalysts for thermal catalytic oxidation of VOCs, such as benzene and toluene, due to the strong interactions between Cu and Ce species [19,20]. However, the combination of Cu–Ce oxide catalysts with non-thermal plasmas for the oxidation of VOCs has not yet been reported [21]. It is still not clear how the interactions between Cu and Ce species will affect the plasma-catalytic oxidation process.

In this study, a series of Cu–Ce oxide catalysts with different molar ratios have been prepared by a citric acid method. The effect of these catalysts on plasma-catalytic removal of formaldehyde as a function of specific energy density (SED) has been investigated in terms of formaldehyde removal efficiency and $CO_2$ selectivity. Catalyst characterization has been carried out using a wide range of analytic techniques such as Brunauer -Emmett -Teller (BET) surface measurement, X-ray diffraction (XRD) and X-ray photoelectron spectroscopy (XPS) to get a better understanding of the roles of these catalysts in the plasma-catalytic process. Plausible reaction mechanisms and pathways have also been proposed and discussed.

## 2. Experimental

### 2.1. Experimental setup

Fig. 1 shows the schematic diagram of the experimental setup. A 60 mm-long aluminum foil (ground electrode) was wrapped over a quartz tube with an inner diameter of 8 mm and wall thickness of 1 mm. A stainless steel rod with an outer diameter of 4 mm was placed in the axis of the quartz tube and acted as a high voltage electrode. As a result, the length of the discharge zone was 60 mm with a discharge gap of 2 mm. Catalysts (100 mg, 35–60 mesh) were packed in the discharge region and held by quartz wool, corresponding to a gas hourly space velocity (GHSV) of 600,000 mL $g^{-1}$ $h^{-1}$. In this study, simulated dry air was used as carrier gas. Gaseous formaldehyde was acquired by feeding a dry air stream through paraformaldehyde powders (99.9%, Alfa Aesar)

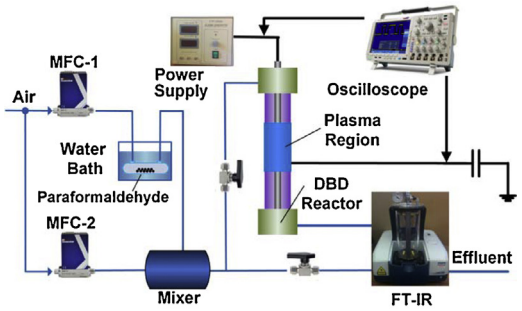


**Fig. 1.** Schematic diagram of the experimental setup.

which were contained in a vessel heated in a water bath (60 °C). The total flow rate for the experiments was fixed at 1 L $min^{-1}$ with a corresponding residence time of 0.23 s in the discharge area. The initial concentration of formaldehyde was kept at 57.7 ppm.

The DBD reactor was supplied by an AC high voltage power supply with a maximum peak voltage of 30 kV and a frequency of 10 kHz. A high voltage probe (Testec, HVP-15HF, 1000:1) was used to measure the applied voltage of the discharge, while a Tektronix P5100 probe was used to measure the voltage across the external capacitor $C_{ext}$ (0.47 μF). All the electrical signals were monitored by a digital oscilloscope (Tektronix 3034B). V–Q Lissajous method was used to calculate the discharge power ($P$) of the DBD reactor. In the present work, specific energy density has been defined as energy dissipated to the plasma per unit volume:

$$\mathrm{SED(J/L)} = \frac{P(W)}{Q(L/\mathrm{min})} \times 60$$

where $P$ is the discharge power and $Q$ is the total flow rate.

Effluent compositions were analyzed online using a Fourier transform infra-red (FTIR) spectrometer (Jasco FT/IR-4200, resolution of 2 $cm^{-1}$) equipped with a 1–16 m variable gas cell (PIKE Technologies). The effective pathlength of the gas cell used in this study was 5.3 m. Measurements were carried out after running the plasma system for about 40 min, when a steady-state had been reached. All the signals were obtained by averaging 128 scans. Quantitative analysis was carried out by comparing the obtained signals with the standard FTIR spectra from Pacific Northwest National Laboratory (PNNL) database. The removal efficiency of formaldehyde is defined as:

$$\eta_{\mathrm{HCHO}} = \frac{C_{in} - C_{out}}{C_{in}} \times 100\%$$

where $C_{in}$ and $C_{out}$ are inlet and outlet concentrations of formaldehyde, respectively.

The selectivity of carbon dioxide ($CO_2$) is defined as follows:

$$\mathrm{CO_2 selectivity(\%)} = \frac{C_{co_2}}{C_{co} + C_{co_2}} \times 100\%$$

where $C_{co}$ and $C_{co_2}$ are CO and $CO_2$ concentrations in the effluent, respectively.

### 2.2. Model description

A Boltzmann equation solver called BOLSIG+ was used to calculate the electron energy distribution in the plasma together with the energy deposition in various electron-induced collisions [22,23]. Based on the classical two term approximation, BOLSIG+ provided steady solutions to the Boltzmann equation in the selected range of the reduced electric field ($E/N$, ratio of electric field to the number density of carrier gas molecules, in Td) and gave outputs of the corresponding electron energy distribution function (EEDF),

mean electron energy, reaction rate coefficients and energy fractions of each plasma reaction channel. The reduced electric field was obtained from the experimental data, while an electron number density of $10^{19}$ $m^{-3}$ was chosen as the initial condition for the calculation, which was within the same order of magnitude of experimental results ($10^{18}$–$10^{21}$ $m^{-3}$) of air DBDs [24,25]. The cross section data of $N_2$ and $O_2$ used in this study was obtained from Phelps and Pitchford [26] and Lawton and Phelps [27], while the effect of formaldehyde was excluded due to its low concentration (57.7 ppm) in the air flow (79% $N_2$ and 21% $O_2$). A list of chosen reactions has been given in Table S1 (Supporting information).

### 2.3. Catalysts preparation

A series of Cu–Ce mixed oxides with different Cu/Ce molar ratios (1:3, 1:1 and 3:1) were prepared using the citric acid method. The desired amount of copper nitrate, ceria nitrate and citric acid (99.9%, Alfa Aesar) was mixed and then dissolved in deionized water. The molar ratio of citric acid to metal salts was 1.5. The above solution was stirred at room temperature for 2 h, followed by drying in a water bath at 80 °C. The obtained samples were heated overnight at 110 °C and then calcined at 500 °C for 5 h. All the catalysts were sieved in 35–60 meshes for testing. Pure copper oxide and ceria oxide were prepared using a similar procedure.

### 2.4. Catalyst characterization

$N_2$ adsorption and desorption experiments were carried out to determine the specific surface area, pore size distribution and average pore diameter of the catalysts using an Autosorb-1-C instrument (Quantachrome Instrument Crop.). XRD patterns of the catalyst samples were recorded by a Rigaku D/max 2550PC system with a Cu-Kα radiation in the $2\theta$ range from 10° to 80°. X-ray photoelectron spectroscopy spectra were recorded with a Thermo ESCALAB 250 using Al Kα X-ray ($h\nu$ = 1486.6 eV) at 150 W as a radiation source. Sample charging effect was eliminated by correcting the observed spectra with the C 1s binding energy (B. E.) value of 284.6 eV. Carbon deposition on the surface of spent catalysts was evaluated by thermogravimetric analysis (TGA) and differential thermal analysis (DTA) in an air atmosphere using a Thermal MAX 500 instrument at a heating rate of 10 °C $min^{-1}$ from 20 °C to 900 °C.

## 3. Results and discussions

### 3.1. Catalyst properties

#### 3.1.1. Structure of Cu–Ce catalysts

The isotherms of nitrogen adsorption/desorption for all the samples are of type IV, which is associated with capillary condensation in mesopores [28]. Type H3 hysteresis loops are observed closing at $P/P_0$ = 0.4 for all the catalysts, which indicate typical open slit-shaped pores with parallel walls and ink-bottle-shaped pores [29]. Table 1 shows the specific surface area ($S_{BET}$), total pore volume and average pore diameter of all the fresh catalysts. A synergy resulting from the interactions between Cu and Ce species can be clearly observed. The specific surface area (33.0–64.4 $m^2$ $g^{-1}$) of the Cu–Ce catalysts is significantly enhanced compared to that of pure CuO (3.6 $m^2$ $g^{-1}$) and $CeO_2$ (10.3 $m^2$ $g^{-1}$). The highest $S_{BET}$ and total pore volume were obtained for the Cu1Ce1 catalyst, while further increasing of the amount of Cu or Ce resulted in a decrease of the $S_{BET}$ and pore volume of the catalysts.Fig. 2 presents the XRD patterns of the fresh and spent catalysts. For the CuO catalyst, typical diffraction patterns of CuO phase (JCPDS 45-0937) can be clearly seen, while the CeO2 and all fresh Cu-Ce catalysts show a typical cubic fluorite-type oxide structure (JCPDS 34-0394). No obvious

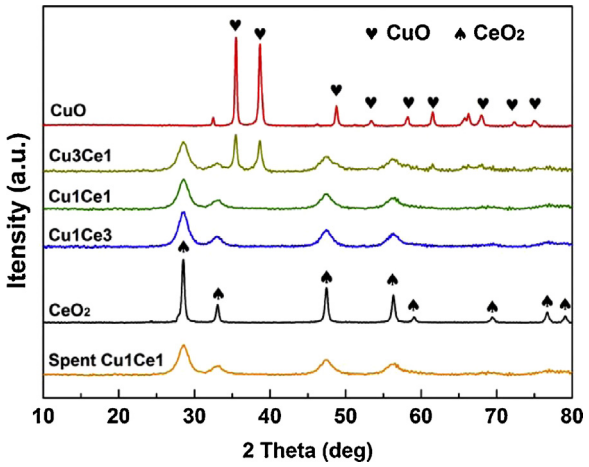


**Fig. 2.** XRD patterns of fresh and spent catalysts.

reflections of a copper oxide phase are found in the Cu1Ce1 and Cu1Ce3 samples, which can be attributed to the well dispersed CuO on the surface of CeO2 [30]. Further increasing of the Cu content leads to the formation of bulk CuO particles, since the characteristic peaks of CuO at $2\theta$ = 35.5° and 38.5° are detected in the Cu3Ce1 catalyst. The diffraction peaks of all the Cu–Ce catalysts are broader compared to those of CuO and CeO2, while the peak intensities of the Cu–Ce catalysts are smaller, indicating the decrease of CeO2 crystallinity by Cu doping, which is in accordance with the calculated crystalline size of CeO2 (Table 1) using the Scherrer's equation [31]

$$d = \frac{0.89\lambda}{(\beta - \beta_o)\mathrm{Cos}\,\theta}$$

where $d$ is the average volume diameter of the crystallite, $\lambda$ is the wavelength of the incident X-rays from the Cu source, $\theta$ is the X-ray incidence angle with respect to the sample surface, $\beta$ is the peak width at half peak height (in radians) and $\beta_0$ is the instrumental line broadening.

Pure $CeO_2$ and CuO have a crystallite size of 17.44 nm and 25.43 nm, respectively, but it decreases significantly to 4.58–5.12 nm in the case of the Cu–Ce catalysts, which is in an agreement with the results of $N_2$ adsorption–desorption experiments in this study. The XRD patterns of the Cu–Ce catalysts show a slight shift of about +0.3° for the characteristic peak of $CeO_2$ (1 1 1) crystal face located at $2\theta$ = 28.5°. This behavior can be explained by the incorporation of CuO into the $CeO_2$ lattice and the partial substitution of Ce cations by Cu cations. Since the radius of $Cu^{2+}$ (0.73 Å) is smaller than that of $Ce^{4+}$ (0.97 Å), a contraction of the $CeO_2$ lattice would occur when $Ce^{4+}$ is replaced by $Cu^{2+}$, as confirmed by the decrease of the lattice constant in Table 1.

#### 3.1.2. Surface analysis of Cu–Ce catalysts

XPS technique has been used to gain a better insight into the chemical states of all the elements on the surface of the Cu–Ce catalysts. Fig. 3 shows the XPS spectra of Cu 2p, Ce 3d and O 1s. The Cu 2p (Fig. 3a) spectra show a main peak of Cu $2p_{3/2}$ at around 934.0 eV, along with the shake-up peaks at 940–945 eV for all the Cu–Ce catalysts. The presence of the shake-up peaks and their binding energy demonstrate the existence of $Cu^{2+}$ species on the catalyst surface [32]. Deconvolution of Cu $2p_{3/2}$ shows two peaks centered at 934.2 and 932.6 eV, respectively. The former can be identified as $Cu^{2+}$ species, while the latter one belongs to a reduced Cu species ($Cu^0$ or $Cu^+$). It is difficult to distinguish the exact chemical state of the reduced surface Cu species using XPS, since the binding energy of these two species is very close. However, it is believed that $Cu^+$

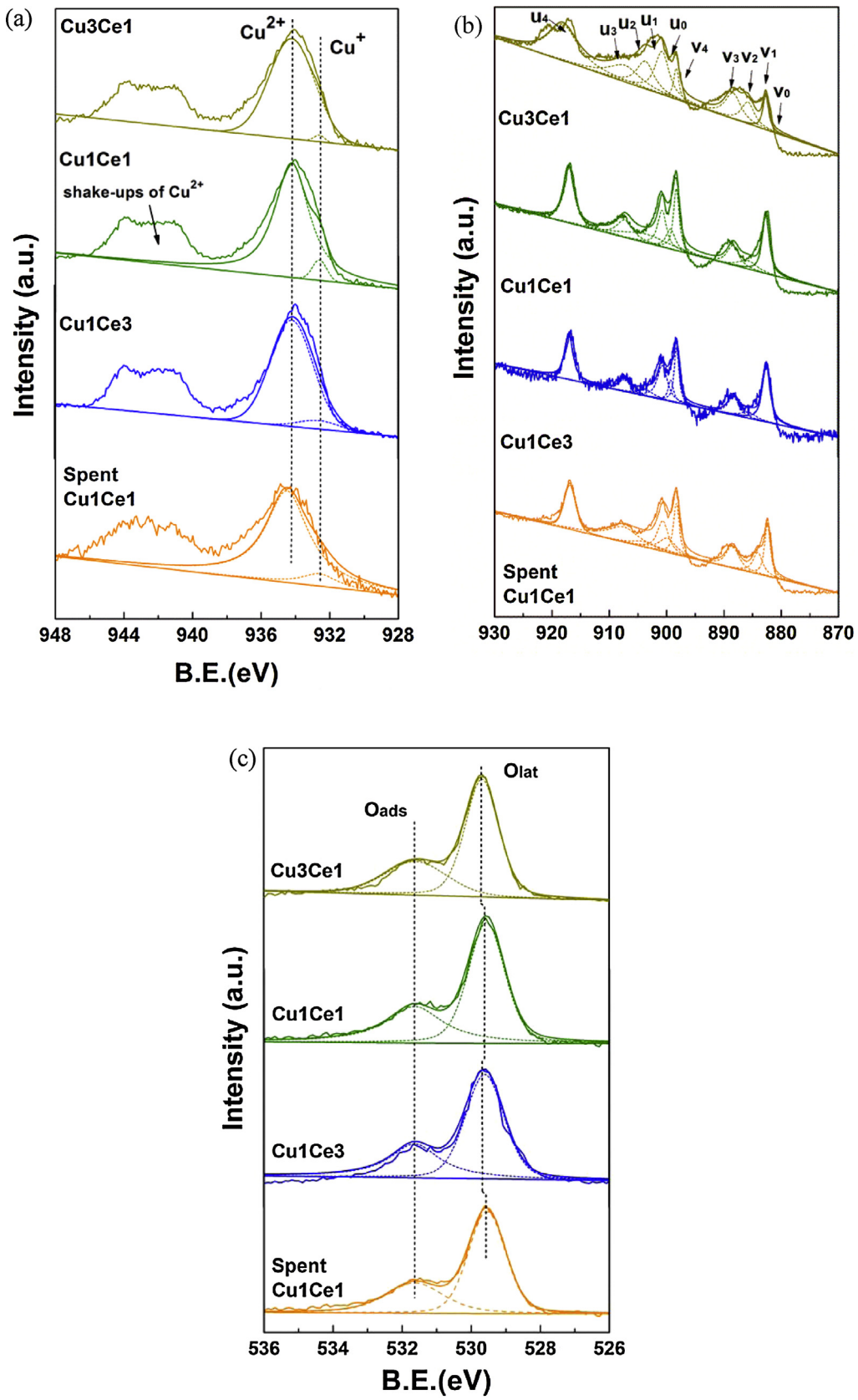


**Fig. 3.** XPS spectra of fresh and spent Cu–Ce binary catalysts (a) Cu 2p; (b) Ce 3d; (c) O 1s.

**Table 1**
Physicochemical characteristics of the catalysts.

| Sample | $S_{BET}$ ($m^2\ g^{-1}$) | Total pore volume ($cm^3\ g^{-1}$) | Average pore diameter (nm) | Crystallite size[a](nm) | Lattice constant[b] (Å) | $Ce^{3+}/Ce^{3+}+Ce^{4+}$[c](%) | $O_{ads}/O_{ads}+O_{lat}$[d](%) |
|---|---|---|---|---|---|---|---|
| CuO | 3.6 | 0.01 | 8.4 | 25.43 | – | – | – |
| Cu3Ce1 | 33 | 0.044 | 6.7 | 5.12 | 5.4095 | 19.94 | 34.05 |
| Cu1Ce1 | 64.4 | 0.081 | 4.4 | 4.58 | 5.4097 | 24.54 | 38.22 |
| Cu1Ce3 | 41.7 | 0.063 | 6.2 | 4.77 | 5.41 | 14.55 | 36.12 |
| $CeO_2$ | 10.3 | 0.035 | 7.7 | 17.44 | 5.4104 | 9.78 | 26.7 |
| Spent Cu1Ce1 | 60.8 | 0.078 | 4.8 | 4.58 | 5.4097 | 23.87 | 33.02 |

[a] All column data correspond to crystallite size of $CeO_2$ except for the first one, which corresponds to CuO.
[b] Calculated from the characteristic peak of $CeO_2$ (1 1 1) crystal face located at $2\theta = 28.5^\circ$ in the XRD patterns.
[c] Relative percentage of $Ce^{3+}$ on catalyst surface is calculated from XPS data.
[d] Relative percentage of surface oxygen species ($O_{ads}$) is calculated from XPS data, while $O_{lat}$ is lattice oxygen species of Cu–Ce catalysts.

rather than $Cu^0$ exists as the main reduced Cu species on the catalyst surface, since these catalysts were calcined in air [33]. $Cu^+$ species can also be formed from the substitution at the interfaces of the oxide phases due to the similar radius of $Cu^+$ and $Ce^{4+}$ ions [30].

The XPS spectra of Ce 3d show the spin-orbit splitting of Ce $3d_{5/2}$ and Ce $3d_{3/2}$, labeled as $u$ and $v$, respectively (Fig. 3b). The spectra can be divided into ten peaks. The $u_2$, $u_0$, $v_2$ and $v_0$ peaks are assigned to $Ce^{3+}$, while the rest belong to $Ce^{4+}$ [34]. The relative concentration of $Ce^{3+}/(Ce^{3+}+Ce^{4+})$ ranges from 14.55% to 24.54% for the Cu–Ce catalysts, which suggests that $CeO_2$ is the main Ce species on the surface of the Cu–Ce catalysts. The XPS spectra of O 1s are shown in Fig. 3c. Two components are identified by deconvoluting the main peak at around 531 eV. The peaks at 529.6 eV are identified as lattice oxygen ($O^{2-}$) (denoted as $O_{lat}$), while those at 531.6 eV are assigned to the surface adsorbed oxygen (denoted as $O_{ads}$) [35]. The relative concentration of $O_{ads}$ ranges from 34.05% to 38.22% as shown in Table 1, suggesting that lattice oxygen is the most abundant oxygen species on the surface of the Cu–Ce catalysts.

### 3.2. Plasma-catalytic removal of formaldehyde

Fig. 4 shows the effect of the Cu–Ce catalysts on the removal of formaldehyde as a function of SED. The removal of formaldehyde increases with increasing SED regardless of the catalyst used. Increasing the SED by raising the applied voltage is expected to effectively enhance the reduced electric field ($E/N$), which changes the electron energy distribution function (EEDF) and enhances the mean electron energy. This can be demonstrated by our calculation through solving the Boltzmann equation using BOLSIG+. Taking the Cu1Ce1 catalyst for example, increasing the applied voltage (peak-to-peak) from 4.86 kV to 6.48 kV significantly increases the SED from 288 $J\,L^{-1}$ to 486 $J\,L^{-1}$, which enhances the reduced electric field from 90 Td to 120 Td and consequently increases the mean electron energy from 2.28 eV to 3.29 eV (shown in Fig. 5a). It is also found that by increasing the SED, the EEDF shifts with an increase in electron density in the high-energy tail of the distribution function (Fig. 5b). It is expected that increasing the SED also leads to an increase in the number of microdischarges per half cycle of the applied voltage. Although it is difficult to quantify the total number of microdischarges in a DBD system, previous work of Kim and Ogata has demonstrated through the use of an intensified charge coupled device (ICCD) camera that increasing the discharge power enhances the electric field, with the formation of more microdischarges in the plasma [36]. Snoeckx et al. have simulated the process of plasma-based dry reforming and found the number of micro-discharge pulses per half cycle has a great influence on the electron density, which in turn affects the calculated conversion and selectivity of the plasma process [25]. As a result of the combined effects induced by the increase of the SED, more

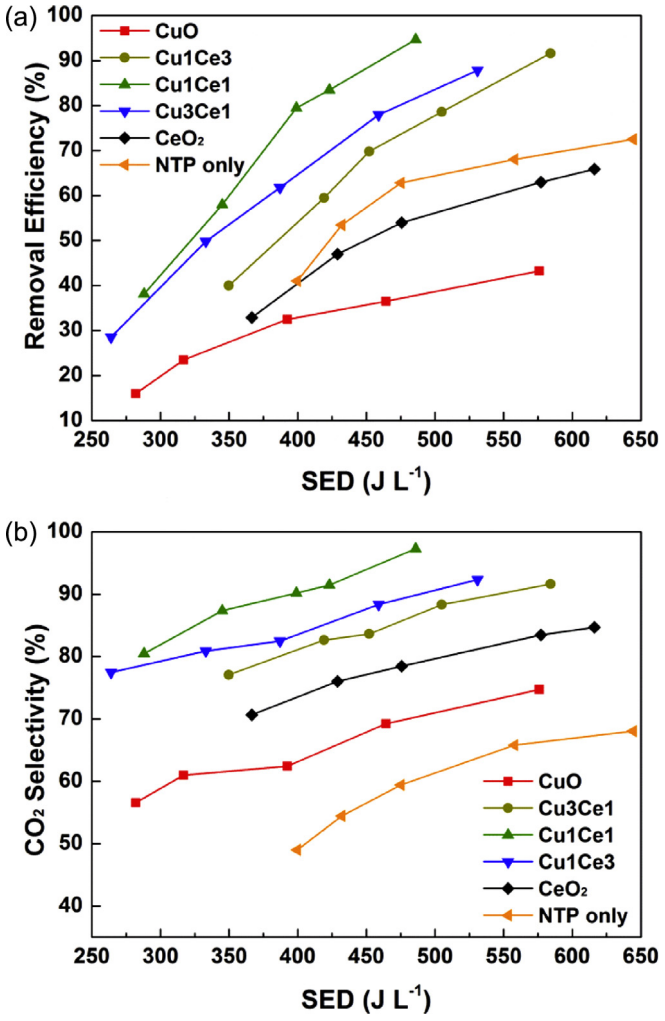


**Fig. 4.** Effect of different catalysts on (a) removal efficiency of formaldehyde; (b) $CO_2$ selectivity as a function of SED.

chemically reactive species can be generated in the discharge via electron impacts to drive the plasma chemical reactions.

To get a better understanding of the initial steps of plasma chemistry, the effect of the reduced electric field on the fraction of energy transferred to different electron-molecule collision channels (e.g., elastic, rotational and vibrational excitations, electronic excitations and ionization) has been investigated (shown in Fig. 5c). In the $E/N$ range of 90 Td to 120 Td, the discharge energy is mainly consumed by electronic, rotational and vibrational excitations. Electronic excitations become more important with increasing $E/N$ as its energy fraction increases from 31.0% to 53.6%. Meanwhile, the

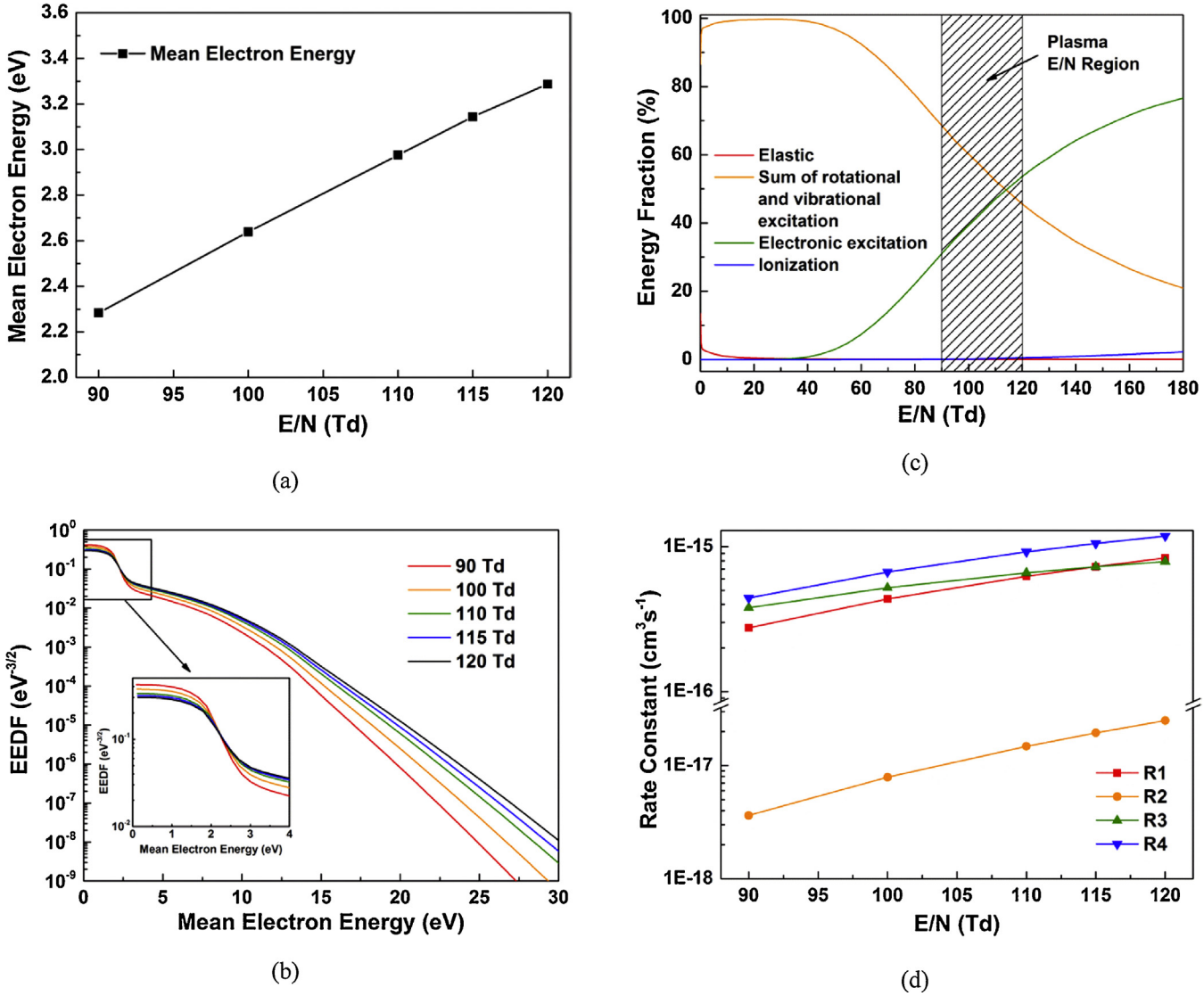


**Fig. 5.** (a) Calculated mean electron energy; (b) EEDF; (c) energy fraction consumed in different electron impact reactions; (d) rate constants of reactions for the formation of N and O radicals in the plasma-catalysis system over the Cu1Ce1 catalyst (*E*/*N*: 90–120 Td; SED: 288–486 J $L^{-1}$).

discharge power consumed by the rotational and vibrational excitation channels is decreased from 68.6% to 45.6%. Only ~2.5% and ~0.3% of the energy contributes to the minor channels of elastic and ionization reactions, respectively. Electronic excitation reactions contribute to the generation of N and O radicals and metastable $N_2$ via R1–R4 [24]:

$$e + N_2 \rightarrow e + N_2(A), N_2(a') \quad \text{R1}$$

$$e + N_2 \rightarrow e + N + N \quad \text{R2}$$

$$e + O_2 \rightarrow e + O + O \quad \text{R3}$$

$$e + O_2 \rightarrow e + O + O(^1D), O(^1S) \quad \text{R4}$$

where $N_2(a')$ denotes the sum of $N_2$ metastable state of $N_2(a'^1\Sigma)$, $N_2(a^1\Pi)$ and $N_2(w^1\Delta)$.

As shown in Fig. 5d, the rate coefficient of the Reactions R1–R4 is enhanced with the increase in SED, resulting in the formation of more reactive species. The reactive species with sufficient energy could collide and react with pollutant molecules. The rotational and vibrational excited $N_2$ and $O_2$ with insufficient energy are not able to rupture the pollutant molecules, but $O_2$ species may play a role in the oxidation of the intermediates to $CO_2$ and $H_2O$ [24].

Compared to the plasma process with no catalyst, the combination of plasma with the Cu–Ce binary catalysts significantly enhances the removal efficiency of HCHO, while the presence of CuO or $CeO_2$ in the DBD reactor has a negative effect on the removal of HCHO. In addition, all the catalyst samples show an enhanced $CO_2$ selectivity when combined with the plasma. The highest formaldehyde removal efficiency (94.7%) and $CO_2$ selectivity (97.3%) were achieved using the Cu1Ce1 catalyst at the SED of 486 J $L^{-1}$, as shown in Fig. 4. These results suggest that the interactions between Cu and Ce species could change the properties of the catalysts, and consequently enhance the performance of the plasma-catalytic oxidation of formaldehyde. As shown in Table 1, the Cu–Ce catalysts have a larger specific surface area and pore volume compared to the pure CuO and $CeO_2$ samples. It is generally recognized that adsorption is the initial step of heterogeneous catalysis. Higher adsorption capacity is expected for the Cu–Ce catalysts due to their larger specific surface area which can provide more adsorption sites and prolong the retention time of formaldehyde in the plasma due to the diffusion of pollutants within the pores. In a single-stage plasma-

catalysis system where the catalyst is directly in contact with the plasma, reactive species can also be generated in the pores of the catalysts; thus, the probability of reactions between the adsorbed pollutant molecules and reactive species in the plasma-catalysis system is enhanced [37]. Guaitella et al. found that the adsorption of $C_2H_2$ and active species increased with increasing catalyst porosity, which led to a higher oxidation of $C_2H_2$ in the plasma-catalytic reactions [38]. These results are in good agreement with the findings of this work as the specific surface areas and pore volumes follow the same order as the removal efficiency and $CO_2$ selectivity: Cu1Ce1 > Cu3Ce1 > Cu1Ce3. It is worth noting that high removal efficiency of 92.9% and $CO_2$ selectivity of 96.4% are achieved in the plasma-catalytic removal of HCHO over the Cu1Ce1 catalyst at a SED of 486 J $L^{-1}$ after reaction for 5 h, showing the satisfied activity and stability of the Cu1Ce1 catalyst under the experimental conditions. The carbon deposition (calculated from the TGA curve) on the spent Cu1Ce1 catalyst after 5 h reaction at the SED of 486 J $L^{-1}$ was 0.15%. This weak coke formation could be the reason for the slightly decreased removal efficiency and $CO_2$ selectivity. The specific surface area and pore volume of the spent Cu1Ce1 catalyst were found to have weakly decreased after the reaction, while the average pore diameter of the catalyst was slightly increased, as shown in Table 1. These changes could be attributed to the block of micro-pores on the Cu1Ce1 catalyst by the carbon deposition. The XRD pattern of the spent Cu1Ce1 catalyst (Fig. 2) shows no significant differences compared to that of the fresh catalyst, indicating the crystallite structure of the catalyst is not changed by the plasma treatment [39].

Previous studies reported the formation of oxygen vacancies on the surface of Cu–Ce catalysts [40,41]. It is believed that the oxygen vacancies act as adsorption–desorption centers for gas phase oxygen species, which favors the generation of surface adsorbed oxygen species ($O_{ads}$) on the Cu–Ce catalysts for the oxidation of formaldehyde [42]. The presence of $Ce^{3+}$ on the surface of the Cu–Ce catalysts confirms the formation of oxygen vacancies. The relative concentration of $Ce^{3+}$ in the Cu–Ce catalysts is found to be much higher than that of pure $CeO_2$ (9.78%), while the Cu1Ce1 catalyst shows the highest $Ce^{3+}$ concentration, which perfectly matches the reaction performance of the plasma-catalytic process. Note that the partial substitution of $Ce^{4+}$ by $Cu^{2+}$ could also lead to the formation of oxygen vacancies or the reduction of $Ce^{4+}$ to $Ce^{3+}$ to retain charge balance [43]. The relative concentration of $Ce^{3+}$ in the spent Cu1Ce1 catalyst is slightly less (23.87%) than that of the fresh catalyst (24.54%), indicating that the part of the $Ce^{3+}$ is oxidized to $Ce^{4+}$ during the plasma-catalytic process [44].

Moreover, the Cu—O and Ce—O chemical bonds can be weakened in the Cu–Ce catalysts due to the electron effect to form more reactive oxygen species and enhance their mobility. As confirmed by XPS results of O 1s, the relative concentration of the surface adsorbed oxygen species $O_{ads}$ in the Cu–Ce samples was higher than that of pure $CeO_2$, whilst the highest $O_{ads}$ concentration of 38.22% was observed in the fresh Cu1Ce1 catalyst with the best reaction performance. The concentration of $O_{ads}$ decreased to 33.02% after the plasma reaction of 5 h, which indicates that the surface adsorbed oxygen species play an important role in the oxidation of formaldehyde on the catalyst surface. The presence of a higher concentration of $O_{ads}$ tends to generate more active oxygen species, which could result in a high removal efficiency via surface reactions [41]. A perfect correlation between the reaction performance and the $O_{ads}$ concentration for different catalysts is observed in this work.

The redox properties of the catalysts generated from the interactions between Cu and Ce species play an important role in the oxidation reactions. Previous studies showed that the redox pairs of $Cu^{2+}/Cu^{+}$ and $Ce^{4+}/Ce^{3+}$ were involved in the electron transfer process from $Ce^{4+}$ to $Cu^{2+}$ within the $Cu^{2+}$–O–$Ce^{4+}$ connections in the Cu–Ce catalysts. The $Cu^{2+}$–O–$Ce^{4+}$ connections could bridge the oxygen transfer within the structure and reduce the redox potential of the Cu species, which ensures the improvement of reducibility for both Cu and Ce oxides in the Cu–Ce samples for the plasma-catalytic oxidation reactions [45].

### 3.3. Reaction mechanisms

The main gaseous products from the plasma-catalytic reactions were CO, $CO_2$ and $H_2O$, while minor products such as HCOOH were also observed. Ozone was not detected for any of the catalysts, which might be decomposed due to heating or catalytic decomposition, or consumed in the plasma oxidation process [46]. In this work, the removal of low concentration formaldehyde in the plasma-catalysis system can be attributed to both plasma gas phase reactions and plasma-assisted surface reactions on the catalyst surface. The gas phase reactions for the removal of formaldehyde are mainly induced by plasma generated reactive species such as O, O($^1$D), OH, N and metastable $N_2$, as shown in R5–R7 [47], while the direct electron-impact collisions only weakly affect the reaction due to the low concentration of formaldehyde in the carrier gas.

$$N_2(A), N_2(a') + HCHO \rightarrow N_2 + NHCO + H \quad \text{R5}$$

$$O, O(^1D) + HCHO \rightarrow HCO + OH \quad \text{R6}$$

$$OH + HCHO \rightarrow HCO + H_2O \quad \text{R7}$$

As shown in R5–R7, HCO is the main intermediate from the initial steps of HCHO oxidation. HCO species can be further oxidized by reactive species such as O and O($^1$D) to form end-products CO, $CO_2$ and $H_2O$ [13]. HCOOH is a common byproduct in plasma processing of HCHO [16]. HCOOH may also be formed from the oxidation of HCHO by O and O(1D) R8 or the recombination of HCO with OH R9:

$$HCHO + O, O(^1D) \rightarrow HCHOOH \quad \text{R8}$$

$$HCO + OH \rightarrow HCOOH \quad \text{R9}$$

Plasma-assisted surface reactions also contribute to the oxidation of HCHO, while thermal catalytic activation of HCHO can be ignored due to the relatively low temperature plasma process (<100 °C) used in this study. In this single-stage plasma catalysis system where the Cu–Ce catalysts are directly in contact with the discharge, both HCHO and intermediates from the gas phase reactions can be adsorbed onto the catalyst surfaces. Short-lived active species (e.g., O) generated close to or on the catalyst surface can participate in the surface reactions. It was reported that the adsorption–desorption equilibrium can be significantly influenced by plasma [48]. Vibrational excited species generated in plasma may also promote the adsorption of pollutants onto the catalyst surface at low temperatures [49]. The enhanced adsorption process increases the collision possibility of pollutants and active species, leading to an acceleration of the plasma chemical reactions. The adsorbed species could also react with adjacent reactive oxygen species from oxygen vacancies or gas-phase O atoms, forming intermediates such as HCO and HCOOH, before finally being oxidized to end-products such as $CO_2$ and $H_2O$. Meanwhile, $Cu^{2+}$ sites on the catalyst surface could be reduced to $Cu^{+}$ and re-oxidized to $Cu^{2+}$ by the adsorbed oxygen or the lattice oxygen from $CeO_2$, which suggests $Ce^{4+}$ acts as an oxygen source for the oxidation of HCHO [50]. The consumed oxygen species on the catalysts can be replenished by capturing oxygen molecules and reactive oxygen species generated in the plasma. The fast redox between $Ce^{4+}$ and $Ce^{3+}$ determines the oxygen storage capacity, which is important for the formation of surface oxygen species. Both Cu and Ce are able to shift between various oxidation states,

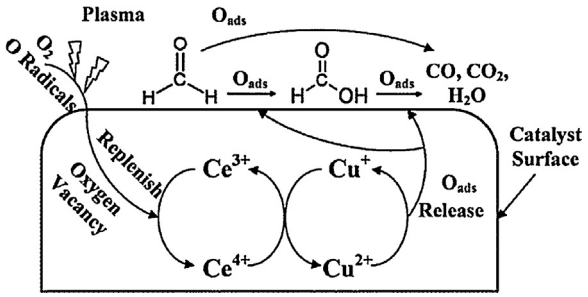


**Fig. 6.** Plausible reaction mechanisms on catalyst surface.

while the interaction between Cu and Ce plays a significant role to enclose the redox reaction cycle, which determines the catalytic performance [45]:

$$Cu^{2+}/Cu^{+} \underset{O^{2-}/O^{-}}{\overset{2e^-}{\rightleftharpoons}} Ce^{4+}/Ce^{3+} \qquad \text{R10}$$

The plausible reaction mechanisms in the plasma-assisted surface oxidation of HCHO are presented in Fig. 6.

## 4. Conclusions

In this study, the effects of the Cu–Ce catalysts and SED on the plasma-catalytic removal of formaldehyde have been investigated in terms of the removal efficiency and $CO_2$ selectivity. Compared to the plasma process in the absence of a catalyst, the presence of CuO or $CeO_2$ catalyst in the plasma decreases the removal efficiency of HCHO, while the combination of plasma with the Cu–Ce binary metal oxide catalysts significantly enhances the reaction performance regardless of the SED. This can be ascribed to the interactions between Cu and Ce species over the catalyst surface. The Cu1Ce1 catalyst (Cu/Ce = 1:1) shows the best reaction performance among all the catalysts with the highest removal efficiency of 94.7% and $CO_2$ selectivity of 97.3% at the SED of 486 J $L^{-1}$. The combination of Cu and Ce oxides results in larger specific surface area and characteristic pore volume and smaller crystalline size, all of which contribute to the plasma-catalytic oxidation of formaldehyde. The interactions between Cu and Ce species also increase the formation of surface adsorbed oxygen species and facilitate the redox cycles between Cu and Ce species, which plays a key role in the plasma-induced surface reactions and significantly improves the removal efficiency of formaldehyde. In this work, the removal of low concentration formaldehyde in the plasma-catalytic process can be attributed to both plasma gas phase reactions and plasma-assisted surface reactions on the catalyst surface.

## Acknowledgements

Support of this work by the Royal Society of the UK (RG120591), the National Natural Science Foundation of China (No. 51076140 & No. 51206143) and the National Science Fund for Distinguished Young Scholars (No. 51125025) is gratefully acknowledged.

## Appendix A. Supplementary data

Supplementary data associated with this article can be found, in the online version, at http://dx.doi.org/10.1016/j.apcatb.2015.01.032.

## References

[1] H.L. Chen, H.M. Lee, S.H. Chen, M.B. Chang, Ind. Eng. Chem. Res. 47 (2008) 2122–2130.
[2] H.H. Kim, Plasma Process. Polym. 1 (2004) 91–110.
[3] R. Aerts, X. Tu, W. Van Gaens, J.C. Whitehead, A. Bogaerts, Environ. Sci. Technol. 47 (2013) 6478–6485.
[4] X. Tu, H.J. Gallon, J.C. Whitehead, J. Phys. D: Appl. Phys. 44 (2011) 482003.
[5] R. Aerts, X. Tu, C. De Bie, J.C. Whitehead, A. Bogaerts, Plasma Process. Polym. 9 (2012) 994–1000.
[6] J. Van Durme, J. Dewulf, C. Leys, H. Van Langenhove, Appl. Catal. B: Environ. 78 (2008) 324–333.
[7] E.C. Neyts, A. Bogaerts, J. Phys. D: Appl. Phys. 47 (2014) 224010.
[8] J.C. Whitehead, Pure Appl. Chem. 82 (2010) 1329–1336.
[9] X. Tu, J.C. Whitehead, Appl. Catal. B: Environ. 125 (2012) 439–448.
[10] X. Tu, H.J. Gallon, M.V. Twigg, P.A. Gorry, J.C. Whitehead, J. Phys. D: Appl. Phys. 44 (2011) 274007.
[11] K. Hensel, Z. Machala, A. Mizuno, 2rd International Workshop on Cold Atmospheric Pressure Plasmas: Sources and Applications, Bruges, Belgium (2005) 85–88.
[12] W.J. Liang, J. Li, J.X. Li, T. Zhu, Y.Q. Jin, J. Hazard. Mater. 175 (2010) 1090–1095.
[13] H.X. Ding, A.M. Zhu, F.G. Lu, Y. Xu, J. Zhang, X.F. Yang, J. Phys. D: Appl. Phys. 39 (2006) 3603–3608.
[14] D.Z. Zhao, X.S. Li, C. Shi, H.Y. Fan, A.M. Zhu, Chem. Eng. Sci. 66 (2011) 3922–3929.
[15] Y. Wan, X. Fan, T. Zhu, Chem. Eng. J. 171 (2011) 314–319.
[16] X. Fan, T. Zhu, Y. Sun, X. Yan, J. Hazard. Mater. 196 (2011) 380–385.
[17] H.L. Tidahy, S. Siffert, F. Wyrwalski, J.F. Lamonier, A. Aboukais, Catal. Today 119 (2007) 317–320.
[18] R. Qu, X. Gao, K. Cen, J. Li, Appl. Catal. B: Environ. 142–143 (2013) 290–297.
[19] S.M. Saqer, D.I. Kondarides, X.E. Verykios, Appl. Catal. B: Environ. 103 (2011) 275–286.
[20] C. Hu, Chem. Eng. J. 168 (2011) 1185–1192.
[21] H.J. Li, X.Y. Jiang, X.M. Zheng, Appl. Surf. Sci. 280 (2013) 273–281.
[22] G.J.M. Hagelaar, L.C. Pitchford, Plasma Sources Sci. Technol. 14 (2005) 722–733.
[23] S. Pancheshnyi, S. Biagi, M.C. Bordage, G.J.M. Hagelaar, W.L. Morgan, A.V. Phelps, L.C. Pitchford, Chem. Phys. 398 (2012) 148–153.
[24] A. Fridman, Plasma Chemistry, Cambridge University Press, 2008.
[25] R. Snoeckx, R. Aerts, X. Tu, A. Bogaerts, J. Phys. Chem. C 117 (2013) 4957–4970.
[26] A.V. Phelps, L.C. Pitchford, Phys. Rev. A 31 (1985) 2932–2949.
[27] S.A. Lawton, A.V. Phelps, J. Chem. Phys. 69 (1978) 1055.
[28] B.C. Lippens, J. De Boer, J. Catal. 4 (1965) 319–323.
[29] K.S. Sing, Pure Appl. Chem. 57 (1985) 603–619.
[30] G. Avgouropoulos, T. Ioannides, H. Matralis, Appl. Catal. B: Environ. 56 (2005) 87–93.
[31] X. Tu, H.J. Gallon, J.C. Whitehead, Catal. Today 211 (2013) 120–125.
[32] D. Mrabet, A. Abassi, R. Cherizol, T.-O. Do, Appl. Catal. A: Gen. 447 (2012) 60–66.
[33] W. Liu, M. Flytzani-Stephanopoulos, J. Catal. 153 (1995) 317–332.
[34] M. Skoda, M. Cabala, I. Matolinova, T. Skala, K. Veltruska, V. Matolin, Vacuum 84 (2009) 8–12.
[35] J.C. Dupin, D. Gonbeau, P. Vinatier, A. Levasseur, Phys. Chem. Chem. Phys. 2 (2000) 1319–1324.
[36] H.H. Kim, A. Ogata, Eur. Phys. J. Appl. Phys. 55 (2011) 13806.
[37] F. Holzer, Appl. Catal. B: Environ. 38 (2002) 163–181.
[38] O. Guaitella, F. Thevenet, E. Puzenat, C. Guillard, A. Rousseau, Appl. Catal. B: Environ. 80 (2008) 296–305.
[39] X. Tang, K. Li, H. Yi, P. Ning, Y. Xiang, J. Wang, C. Wang, J. Phys. Chem. C 116 (2012) 10017–10028.
[40] G. Marbán, A.B. Fuertes, Appl. Catal. B: Environ. 57 (2005) 43–53.
[41] G. Zhou, H. Lan, T. Gao, H. Xie, Chem. Eng. J. 246 (2014) 53–63.
[42] M. Roxana Morales, F.N. Agueero, L.E. Cadus, Catal. Lett. 143 (2013) 1003–1011.
[43] A. Martinezarias, D. Gamarra, M. Fernandezgarcia, X. Wang, J. Hanson, J. Rodriguez, J. Catal. 240 (2006) 1–7.
[44] W. Shan, M. Fleys, F. Lapicque, D. Swierczynski, A. Kiennemann, Y. Simon, P.-M. Marquaire, Appl. Catal. A: Gen. 311 (2006) 24–33.
[45] U. Menon, H. Poelman, V. Bliznuk, V.V. Galvita, D. Poelman, G.B. Marin, J. Catal. 295 (2012) 91–103.
[46] F. Holzer, F.D. Kopinke, U. Roland, Plasma Chem. Plasma Process. 25 (2005) 595–611.
[47] N. Blin-Simiand, S. Pasquiers, F. Jorand, C. Postel, J.R. Vacher, J. Phys. D: Appl. Phys. 42 (2009) 122003.
[48] N. Blin-Simiand, P. Tardiveau, A. Risacher, F. Jorand, S. Pasquiers, Plasma Processes Polym. 2 (2005) 256–262.
[49] T. Nozaki, H. Tsukijihara, W. Fukui, K. Okazaki, Energy Fuels 21 (2007) 2525–2530.
[50] C. He, Y. Yu, C. Chen, L. Yue, N. Qiao, Q. Shen, J. Chen, Z. Hao, RSC Adv. 3 (2013) 19639.